

AD-A106 097

MISSION RESEARCH CORP LA JOLLA CA  
HIGH DOSE RATE ELECTRON BEAM TESTING. (U)  
DEC 80 T F WROBEL

F/G 18/B

UNCLASSIFIED

MRC/SD-R-68

DNA-5542F

DNA001-80-C-0140

NL

1 of 1  
AD-A106 097




END  
DATE  
SUBMIT  
11-81  
DTIC

AD A106097

# HIGH DOSE RATE ELECTRON BEAM TESTING

T. F. Wrobel  
Mission Research Corporation  
P.O. Box 1209  
La Jolla, California 92038

1 December 1980

Final Report for Period 1 March 1980—30 September 1980

CONTRACT No. DNA 001-80-C-0140

APPROVED FOR PUBLIC RELEASE;  
DISTRIBUTION UNLIMITED.

DTIC  
ELECTE  
OCT 27 1981

A

THIS WORK SPONSORED BY THE DEFENSE NUCLEAR AGENCY  
UNDER RDT&E RMSS CODES B323080464 X99QAXVB20102 H2590D  
AND X323080469 Q31QAXVB20201 H2590D.

DTIC FILE COPY

Prepared for  
Director  
DEFENSE NUCLEAR AGENCY  
Washington, D. C. 20305

81 10 26 064

Destroy this report when it is no longer  
needed. Do not return to sender.

PLEASE NOTIFY THE DEFENSE NUCLEAR AGENCY,  
ATTN: STTI, WASHINGTON, D.C. 20305, IF  
YOUR ADDRESS IS INCORRECT, IF YOU WISH TO  
BE DELETED FROM THE DISTRIBUTION LIST, OR  
IF THE ADDRESSEE IS NO LONGER EMPLOYED BY  
YOUR ORGANIZATION.



UNCLASSIFIED

SECURITY CLASSIFICATION OF THIS PAGE (When Data Entered)

REPORT DOCUMENTATION PAGE		READ INSTRUCTIONS BEFORE COMPLETING FORM
1. REPORT NUMBER DNA/5542F	2. GOVT ACCESSION NO. 4D-A106097	3. RECIPIENT'S CATALOG NUMBER
4. TITLE (and Subtitle) HIGH DOSE RATE ELECTRON BEAM TESTING		5. TYPE OF REPORT & PERIOD COVERED Final Report for Period 1 Mar 80-30 Sep 80
7. AUTHOR(s) T. F. Wrobel		8. PERFORMING ORG. REPORT NUMBER MRC/SD-R-68
9. PERFORMING ORGANIZATION NAME AND ADDRESS Mission Research Corporation P.O. Box 1209 La Jolla, California 92038		6. CONTRACT OR GRANT NUMBER(s) DNA 001-80-C-0140
11. CONTROLLING OFFICE NAME AND ADDRESS Director Defense Nuclear Agency Washington, D.C. 20305		10. PROGRAM ELEMENT PROJECT, TASK AREA & WORK UNIT NUMBERS Subtasks X99QAXVB201-02 Q31QAXVB202-01
14. MONITORING AGENCY NAME & ADDRESS (if different from Controlling Office)		12. REPORT DATE 1 December 1980
		13. NUMBER OF PAGES 46
		15. SECURITY CLASS (of this report) UNCLASSIFIED
		15a. DECLASSIFICATION DOWNGRADING SCHEDULE
16. DISTRIBUTION STATEMENT (of this Report) Approved for public release; distribution unlimited.		
17. DISTRIBUTION STATEMENT (of the abstract entered in Block 20, if different from Report)		
18. SUPPLEMENTARY NOTES This work sponsored by the Defense Nuclear Agency under RDT&E RMSS Codes B323080464 X99QAXVB20102 H2590D and X323080469 Q31QAXVB20201 H2590D.		
19. KEY WORDS (Continue on reverse side if necessary and identify by block number) High Dose Rate TLD's HIFX Electron Beam Calorimeters Primary Photocurrent Hermes		
20. ABSTRACT (Continue on reverse side if necessary and identify by block number) A test program was designed to investigate test methods utilized for high dose rate e-beam testing of semiconductor components. Several methods used to vary the exposure dose were investigated including the variation of drift chamber pressure and length as well as beam aperturing. The photo response obtained for a 1N916 diode at the HIFX and Hermes facilities were in agreement for the various modes of apparation. In addition, it was found that acceptable dose measurements can be performed at the high intensities if the dosimeters are placed in close proximity to the device under test.		

DD FORM 1 JAN 73 1473 EDITION OF 1 NOV 65 IS OBSOLETE

UNCLASSIFIED

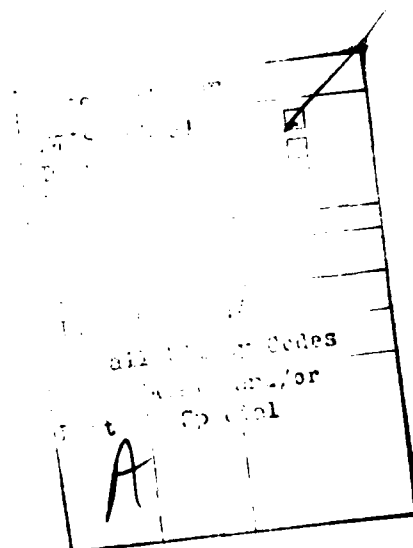
SECURITY CLASSIFICATION OF THIS PAGE (When Data Entered)

312717

JK

## TABLE OF CONTENTS

	<u>Page</u>
LIST OF ILLUSTRATIONS	2
LIST OF TABLES	3
1 INTRODUCTION	5
2 DOSIMETRY	7
3 ELECTRON BEAM TRANSPORT	22
4 CONCLUSIONS	37



## LIST OF ILLUSTRATIONS

<u>Figure</u>		<u>Page</u>
1	A typical high speed, 1 mil foil, thermocouple response from Hermes shot #18233.	13
2	Calorimeter response for a 1 mil and 6 mil foil calorimeter. Hermes shot #18241.	15
3	Beam uniformity measurement at the HIFX facility (dose in rad(Si) $\times 10^4$ ).	16
4	Beam uniformity measurement at the Hermes facility (dose in rad(Si) $\times 10^4$ ).	16
5	Schematic diagram of the test configuration for Hermes Shot #'s 18242 through 18266.	17
6	Comparison between TLD response and the copper calorimeter response.	18
7	Dose variation vs aperture for HIFX-HiVac-160 cm position.	23
8	Dose variation vs aperture size for Hermes.	23
9	Hermes gamma dose vs distance.	23
10	HIFX dose response vs pressure.	24
11	Hermes beam transport response vs pressure (from Sandia data shot #'s 17671 through 17680 + 17668).	25
12	The geometry for multiple scattering through a foil of thickness t.	27
13	Photo response for a long lead measurement circuit.	32
14	Double CT-2 test circuit.	32
15	Double transformer outputs for HIFX shot #3031. Upper trace is transformer 1 and the lower trace is transformer 2.	33
16	Differential photo response for HIFX shot #3052 (lower trace).	33
17	Summary plot of the Hermes and HIFX photo response.	35

## LIST OF TABLES

<u>Table</u>		<u>Page</u>
1	Comparison between the thermocouple and thermistor calorimeter responses for HIFX shot numbers 3022 through 3038. Thermocouple amplifier sensitivity 200x thermistor amplifier sensitivity.	9
2	Comparison between the 1 mil calorimeter and 6 mil calorimeter response at Hermes. Calorimeters spaced 0.25 cm.	14
3	Comparison of copper calorimeter response to the TLD response at HIFX.	17
4	Comparison of copper calorimeter response to the TLD response at Hermes.	19
5	Diode response for electron beam exposure in partial vacuum and atmospheric pressure air.	36

## SECTION 1 INTRODUCTION

The test program described below was designed to investigate test methods for both real time and post exposure electrical characterization of semiconductor components exposed to high dose rate ( $\geq 10^{12}$  rad(Si)/s) Flash X Ray (FXR) electron beam sources. To accomplish this, a test program was developed to investigate methods of testing the devices when exposed in air, vacuum, and partial vacuum with inter-comparisons with photon exposure results. The e-beam results should correlate directly with the photon results. The test devices were exposed at facilities having substantially different outputs with respect to beam current, electron energy and output pulse width, in order to assess any machine parameter effects on the applicable test methods.

The methodology utilized to vary the dose rate at the test part location was investigated. These included the variation in drift chamber length (under high vacuum conditions, the dose at the end of the drift chamber decreases with increasing length), the variation of the chamber gas pressure (the e-beam transport efficiency varied as a function of chamber pressure) and the variation of aperture size (the apertures restrict the amount of beam current transported down the drift chamber). Finally, dosimetry methods were investigated using copper foil thermocouple and thermistor colorimeters and thermoluminescent dosimeters (TLD's) to cover the dose range of 1 Krad(Si) to  $\sim 10^6$  rad(Si).

The program was performed jointly with personnel from AWRE of the United Kingdom, Sandia National Laboratory and Mission Research Corporation. The subject of this report is limited to the beam transport, dosimetry



techniques, the 1N916 diode radiation response, and the test techniques utilized at the Harry Diamond Laboratories HIFX and SNLA Hermes facilities.

At the HIFX facility, the devices were exposed in the bremsstrahlung mode in air at atmospheric pressure, the electron beam mode in air at atmospheric pressure and the electron beam mode in high and partial vacuum. Both electron beam aperturing and the variation of the electron beam drift chamber pressure and length were used to vary the dose exposure levels. The primary photocurrent was recorded over a dose rate range of  $3 \times 10^{10}$  rad(Si)/s to  $6 \times 10^{12}$  rad(Si)/s.

The devices were exposed in the bremsstrahlung and partial vacuum e-beam mode at the Hermes facility. Electron aperturing and drift chamber pressure variation were utilized to vary the dose exposure levels. The photo response was recorded over a dose rate range of  $3.4 \times 10^{11}$  to  $10^{12}$  rad(Si)/s.

In addition a brief section discussing the electron beam transport in a gaseous medium is included in an attempt to explain the differences (dose versus pressure responses) observed at the HIFX and Hermes facilities.

## SECTION 2

### DOSIMETRY

The object of dosimetry is to quantitatively describe a radiation environment. If it is to be useful, a description of the radiation environment must be relevant to the radiation effect being studied. The calorimeters described here were specifically designed for comparison with ionization-induced primary photocurrent in silicon solid-state devices (such as diodes). These thin calorimeters determine the dose by measuring the temperature rise in a small piece of copper. Since the temperature rise can be converted to energy deposition (dose) by the specific heat of copper, the measurement is a direct determination of the average dose in the sample independent of the type of radiation particle or its energy.

Copper was selected because of its good sensitivity, its ease of construction, and the availability of materials. Two types of calorimeters were utilized. One type used a Chromel Alumel thermocouple to measure the temperature rise in the copper and the other type utilized a thermistor as the temperature sensing element. In addition, thermoluminescent dosimeters (TLD's) were also utilized during the program as a cross correlation. A discussion of the calorimeters and a comparison with the TLD results is presented below.

#### CONSTRUCTION

Several factors were taken into account in the design of the calorimeters. They were suspended by styrofoam blocks and the temperature sensing element was attached with a small amount of thermally conductive epoxy. The copper foil was  $\approx 0.6$  cm diameter disc. The calorimeter

measurements at the HIFX facility utilized a  $2.54 \times 10^{-3}$  cm thick foil while the later measurements performed at the Hermes facility included three thicknesses of foil ( $2.5 \times 10^{-3}$  cm,  $1.5 \times 10^{-2}$  cm and  $2.8 \times 10^{-2}$  cm).

### THEORY

Radiation incident upon copper block manifests itself as a temperature rise which can be converted to energy deposition (dose) by the specific heat of copper. The measurement is a direct determination of the average dose in the sample, independent of the type of radiation particle or its energy, and is traceable to NBS standards (NBS Circular 500, Part 1, 1952). The specific heat capacity for copper is 0.092 cal/g/°C at 25°C. This can be directly converted to  $3.85 \times 10^4$  rad(Cu)/°C by using the conversion factor  $4.19 \times 10^7$  erg/cal and 100 erg/g-rad. The response of the chromel-alumel thermocouple at room temperature is  $40 \mu\text{V}/^\circ\text{C} \pm 1 \mu\text{V}/^\circ\text{C}$ . Therefore, the response of our copper calorimeter is 964 rad(Cu)/ $\mu\text{V}$ . The thermistor calorimeter is calibrated against the thermocouple calorimeter and its sensitivity is dependent on the resistance value of the thermistor selected and the measuring circuit. Table 1 lists the comparisons between the thermocouple calorimeter response and the thermistor calorimeter response for HIFX shot number 3022 through 3038. It can be seen from the data that large variations in the thermistor sensitivity exist. This is due to temperature variations in the value of the thermistor resistance which results in a different R vs T response at different temperatures. The ratio of resistance change per unit temperature change divided by the resistance remains approximately constant. Fortunately the sensitivity of the thermocouple calorimeters was sufficient to allow dose measurements down to  $\approx 1 \times 10^3$  rad(Si). The thermistor calorimeters were  $\approx 370$  times more sensitive than the thermocouple calorimeters, resulting in a calibration factor of 2.6 rad(Cu)/ $\mu\text{V}$ .

To be useful for the characterization of silicon semiconductor devices, it is necessary to convert from rad(Cu) to rad(Si). An expression

Table 1. Comparison between the thermocouple and thermistor calorimeter responses for HIFX shot numbers 3022 through 3038. Thermocouple amplifier sensitivity 200x thermistor amplifier sensitivity.

Shot Number	Thermocouple Calorimeter response (rad(Si)/ inch	Thermistor Calorimeter response rad(Si)/inch
3022	$4.25 \times 10^3$	$2.3 \times 10^3$
3023	↓	$2.1 \times 10^3$
3024		$2.2 \times 10^3$
3025		$2.3 \times 10^3$
3026		$2.4 \times 10^3$
3027		$2.4 \times 10^3$
3028		
↓	No Data	
3031		
3032	$4.25 \times 10^3$	$3 \times 10^3$
3033	↓	$2.5 \times 10^3$
3034		$1.8 \times 10^3$
3035		$2.6 \times 10^3$
3036		$3.0 \times 10^3$
3037		$2.1 \times 10^3$
3038		$1.8 \times 10^3$
		$\bar{X} = 2.3 \times 10^3$
		$\sigma = 0.4 \times 10^3$

describing the energy loss by inelastic collision of electrons is given by equation 1 (Ref. 1) for  $E \gg m_0 c^2$ ,

$$\frac{-dE}{dx} = \frac{2\pi N e^4 Z}{m_0 c^2} \left[ \log \left( \frac{E^3}{2 m_0 c^2 I^2} \right) + \frac{1}{8} \right] \quad (1)$$

where  $x$  = path length in centimeters,  
 $N$  = number per cubic centimeter = (Avogadro's # x density ÷ atomic weight),  
 $e$  = electronic charge =  $1.6 \times 10^{-19}$  coulombs,  
 $Z$  = atomic number,  
 $E$  = the electron energy (kinetic),  
 $m_0 c^2$  = electron rest mass energy  $\sim 5.1 \times 10^5$  eV,  
 $I$  = the mean excitation potential = 276 eV for copper,  
and  $I$  = 150 eV for silicon.

Converting the energy loss per cm to energy loss per  $\text{g/cm}^2$  we obtain

$$\frac{-dE}{dx'} = \frac{2\pi N e^4 Z}{m_0 c^2 \rho} \left[ \log \left( \frac{E^3}{2 m_0 c^2 I^2} \right) + \frac{1}{8} \right] \quad (2)$$

where  $x'$  is the path length in  $\text{g/cm}^2$  and  $\rho$  = density of the material in  $\text{gm/cm}^3$ . Since  $N = A \rho / A$  where  $A$  is Avogadro's number and  $A$  is the atomic weight we obtain

$$\begin{aligned} \frac{-dE}{dx'} &= \frac{2\pi A \rho e^4 Z}{A m_0 c^2 \rho} \left[ \log \left( \frac{E^3}{2 m_0 c^2 I^2} \right) + \frac{1}{8} \right] \\ &= K \frac{Z}{A} \left[ \log \left( \frac{E^3}{2 m_0 c^2 I^2} \right) + \frac{1}{8} \right] \end{aligned} \quad (3)$$

1. Experimental Nuclear Physics, Vol. 1, E. Segre, John Wiley & Sons, 1953.

Therefore using

$$\begin{aligned} Z(\text{Cu}) &= 29, \\ Z(\text{Si}) &= 14, \\ A(\text{Cu}) &= 63.54, \text{ and} \\ A(\text{Si}) &= 28.09, \text{ and} \end{aligned}$$

using an average energy of 5 Mev we obtain

$$\frac{\left. \frac{dE}{dx'} \right|_{\text{Cu}}}{\left. \frac{dE}{dx'} \right|_{\text{Si}}} = 0.866 \quad (4)$$

or 1 rad(Si)  $\approx$  1.155 rad(Cu).

An analysis of the heat transfer characteristics between the copper calorimeter and its environment is essential for the design of any calorimetry system. The heat transfer problem can be divided into three distinct phenomena — convection, radiation and conduction.

Convection currents can be substantially eliminated by surrounding the copper disc with styrofoam. Thus, this mode of heat transfer can be reduced to negligible levels when compared to the other modes.

The heat loss by radiation is described by the Stephen-Boltzman relation:

$$H = \epsilon \phi A (T^4 - T_0^4), \quad (5)$$

where

- $\epsilon$  = emissivity of copper  $\approx$  0.05,
- $\phi$  = Stephen-Boltzman constant  $= 1.36 \times 10^{-12} \text{ cal/cm}^2\text{-}^\circ\text{K}^4\text{-s}$ ,
- $T$  = the absolute temperature of the calorimeter after exposure,
- $T_0$  = the absolute temperature of the environment, and
- $A$  = the total area of the sensing element  $= .6 \text{ cm}^2$ .

The temperature rise for a  $\sim 45$  Krad radiation pulse is  $\sim 1^\circ\text{C}$ . Therefore the steady state rate of heat flow per unit time is  $\sim 3 \times 10^{-6}$  cal/s using  $273^\circ\text{K}$  for  $T_0$  and  $274^\circ\text{K}$  for  $T$ .

The transport of heat along a thermal gradient by intermolecular collision is called conductive heat transfer and is given by Fourier's law as

$$H = -K_{th} A \frac{\partial T}{\partial x}, \quad (6)$$

where

$H$  = rate of heat flow (cal/s),

$x$  = length of heat path (cm),

$A$  = cross sectional area available for the flow ( $\text{cm}^2$ ),

$\partial T$  = the temperature gradient ( $^\circ\text{C}/\text{cm}$ ), and

$K_{th}$  = thermal conductivity coefficient [ $(\text{cal-cm})/(\text{cm}^2\text{-s-}^\circ\text{C})$ ].

This equation applies to the temperature sensing element lead wires and also the trapped air between the copper element and the external ambient.

For the chromel-alumel wires used

$$A = 5 \times 10^{-6} \text{ cm}^2,$$

$$K_{th} = .041 \text{ cal-cm/cm}^2\text{-s-}^\circ\text{C},$$

$$\partial x = 0.6, \text{ and}$$

$$\partial T = 1^\circ\text{C}.$$

Therefore, the total heat flow through the leads is,  $H \sim 4.5 \times 10^{-7}$  cal/s for a one degree C temperature rise. Similarly, for the trapped air,

$$A = 0.6 \text{ cm}^2,$$

$$K_{th} = 5.7 \times 10^{-5} \text{ cal-cm/cm}^2\text{-s-}^\circ\text{C},$$

$$\partial x = .12 \text{ cm},$$

$$\partial T = 1^\circ\text{C},$$

and the heat loss  $H \approx 2.9 \times 10^{-4}$  cal/s, again for a  $1^\circ\text{C}$  temperature rise. It is clear from the above that the dominant heat loss mechanism at least for small dose exposures ( $\approx 50$  Krad) is the trapped air.

The theoretical time constant for the calorimeter is given by

$$\tau = \frac{Sh \rho V}{H}, \quad (7)$$

where  $Sh$  is the specific heat ( $.09$  cal/cm- $^\circ\text{C}$ )  $\rho$  is the density of copper ( $8.9$  g/cm $^3$ ),  $V$  is the volume ( $8 \times 10^{-4}$  cm $^3$ ) of the copper disc, and  $H$  is the heat loss rate (cal/s) for a  $1^\circ\text{C}$   $\Delta T$ . This yields a thermal time constant of  $\tau = 2$  s for the 1 mil foil calorimeter,  $\tau = 12$  for a 6 mil foil and 22 s for an 11 mil foil.

A typical high chart speed for 1 mil foil thermocouple response is shown in Figure 1 for Hermes shot number 18233. It is evident from this figure that there are multiple (at least two) thermal decay time constants. The slow decay response was subtracted from the background signal and the initial response decayed with  $\tau \approx 0.4$  s. This is faster than the calculated value of 2 s from above and indicates that the peak of the calorimeter response is the correct point to measure. It is believed that the slow component of the thermal decay is caused by the close proximity of the calorimeters to a large amount of aluminum. The aluminum also rises in temperature and the heat loss from calorimeter foil is reduced due to the reduced  $\Delta T$ . Therefore for longer times the calorimeters will decay as the nearby aluminum decays.

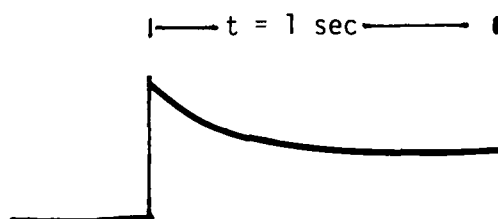


Figure 1. A typical high speed, 1 mil foil, thermocouple response from Hermes shot #18233.



A comparison between the 1 mil and 6 mil foil calorimeter responses and decays was also performed. These results are tabulated in Table 2 and shown in Figure 2. As can be seen there is very good agreement between the peak response of both the foils, further indication that the correct dose is obtained if the peak in the response is read. On a few of the earlier calorimeter records, the noise precluded an accurate measurement of the peak response. Therefore the later data (Table 2) were used to establish the ratio between the peak response and the 1 s response so that the peak response of the earlier noisy data could be obtained from the 1 s response point.

Table 2. Comparison between the 1 mil calorimeter and 6 mil calorimeter response at Hermes. Calorimeters spaced 0.25 cm.

Shot #	Front Calorimeter Dose (rad(Si)) (1 mil, $\tau' \approx 6$ s)*	Rear Calorimeter Dose (rad(Si)) (6 mil, $\tau' \approx 20$ s)*	Ratio F/R
18242	16.8 K	15.6 K	1.08
18243	12 K	13.0 K	.93
18244	14.9 K	14.9 K	1.0
18245	14.9 K	13.9 K	1.07
18246	15.4 K	15.8 K	.97
18247	12 K	11.5 K	1.04
18248	12.5 K	12.5 K	1.00
18249	63.4 K	60 K	1.06
18250	78.7 K	78.7 K	1.00
18251	142 K	125 K	1.14
$* \tau' = - \left( \ln \frac{x_0}{x_1} \right)^{-1}$			$\bar{x} = 1.03$ $\sigma = 0.06$

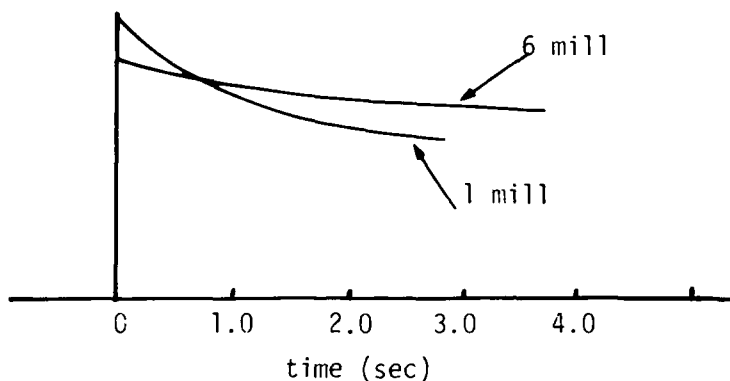


Figure 2. Calorimeter response for a 1 mil and 6 mil foil calorimeter. Hermes shot #18241.

The beam uniformity was measured at the HIFX and Hermes facilities using an array of nine calorimeters arranged in a cross pattern. At the HIFX facility, the beam uniformity was measured at the 15 cm position and at the 160 cm position. These results are shown in Figure 3 where the dose is in rads(Si). A similar measurement was performed at the Hermes facility and these results are shown in Figure 4. As can be seen from these figures, reasonable uniformity, at least on a relatively large scale, was obtained for the operating parameters listed.

A careful comparison between the calorimeter response and the TLD's was performed at the Hermes facility for shot numbers 18242 through 18266. The geometry of the test setup is shown in Figure 5. The results of this comparison are shown plotted in Figure 6 where the average calorimeter dose in rad(Si) is plotted against the average TLD reading. As can be seen the results agree quite well and indicate that a strong correlation can be obtained when they are placed in very close proximity. A summary of the average TLD responses versus the average copper calorimeter response for the HIFX facility tests and for the Hermes facility test are listed in Tables 3 and 4 respectively. These results do not correlate nearly as well and indicate that large spacial variations probably exist in the electron beam field as well as in the gamma ray field since the TLD's were located approximately 1 to 2 cm from the test part center position.

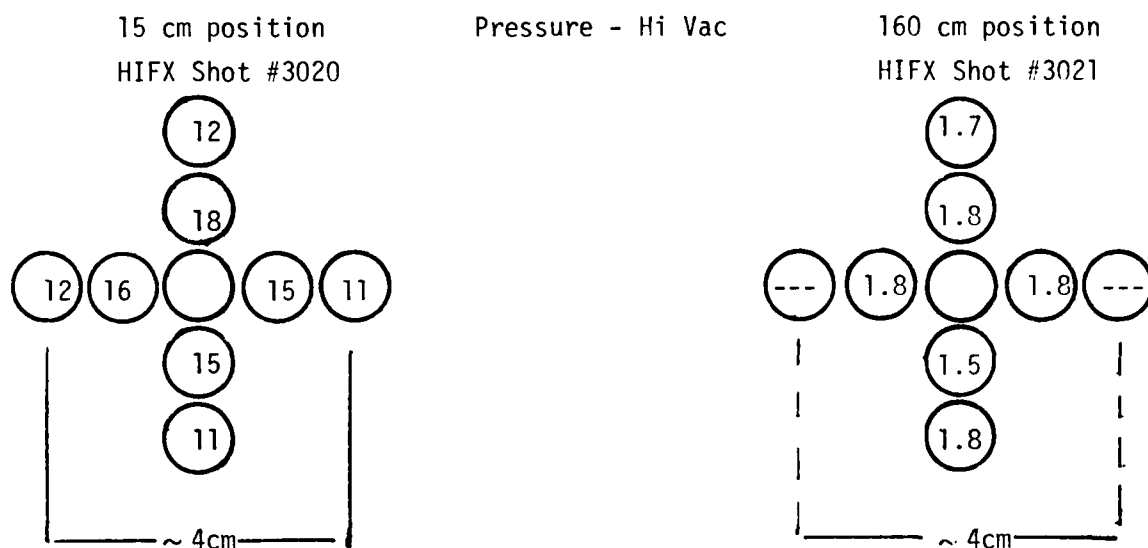


Figure 3. Beam uniformity measurement at the HIFX facility (dose in  $\text{rad(Si)} \times 10^4$ ).

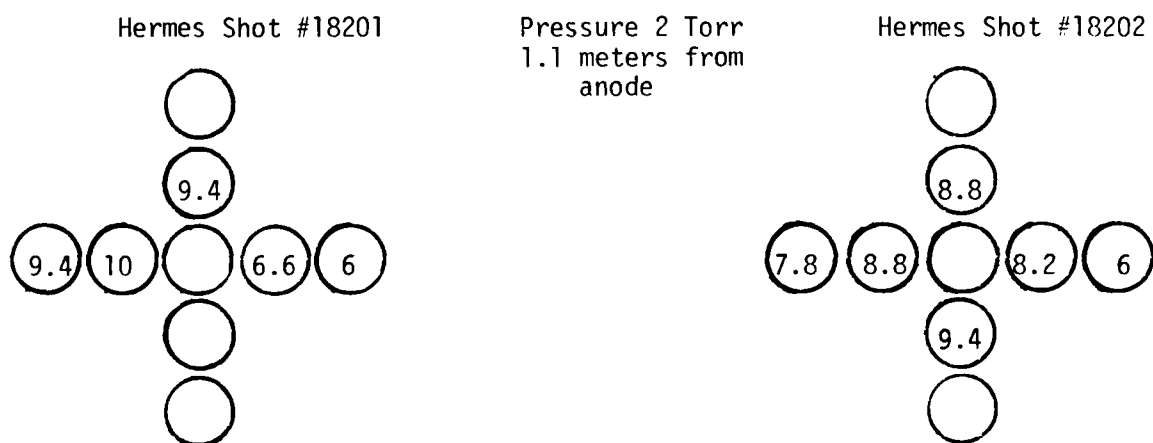


Figure 4. Beam uniformity measurement at the Hermes facility (dose in  $\text{rad(Si)} \times 10^4$ ).

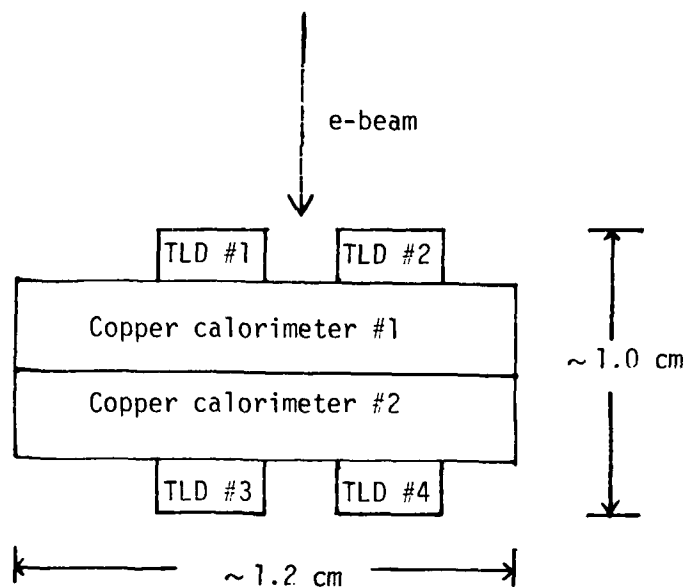


Figure 5. Schematic diagram of the test configuration for Hermes Shot #'s 18242 through 18266.

Table 3. Comparison of copper calorimeter response to the TLD response at HIFX.

Shot #	Copper Calorimeter Dose rad(Si)	TLD Dose rad(Si)
3021	$1.6 \times 10^4$	$1.7 \times 10^4$
3032 + 3033	956	743
3034	722	$1.1 \times 10^3$
3035 + 3036	$1.9 \times 10^3$	$1.9 \times 10^3$
3037	$2.4 \times 10^3$	$2.9 \times 10^3$
3038	$2.0 \times 10^3$	$2.9 \times 10^3$
3040	$2.0 \times 10^4$	$2.4 \times 10^4$

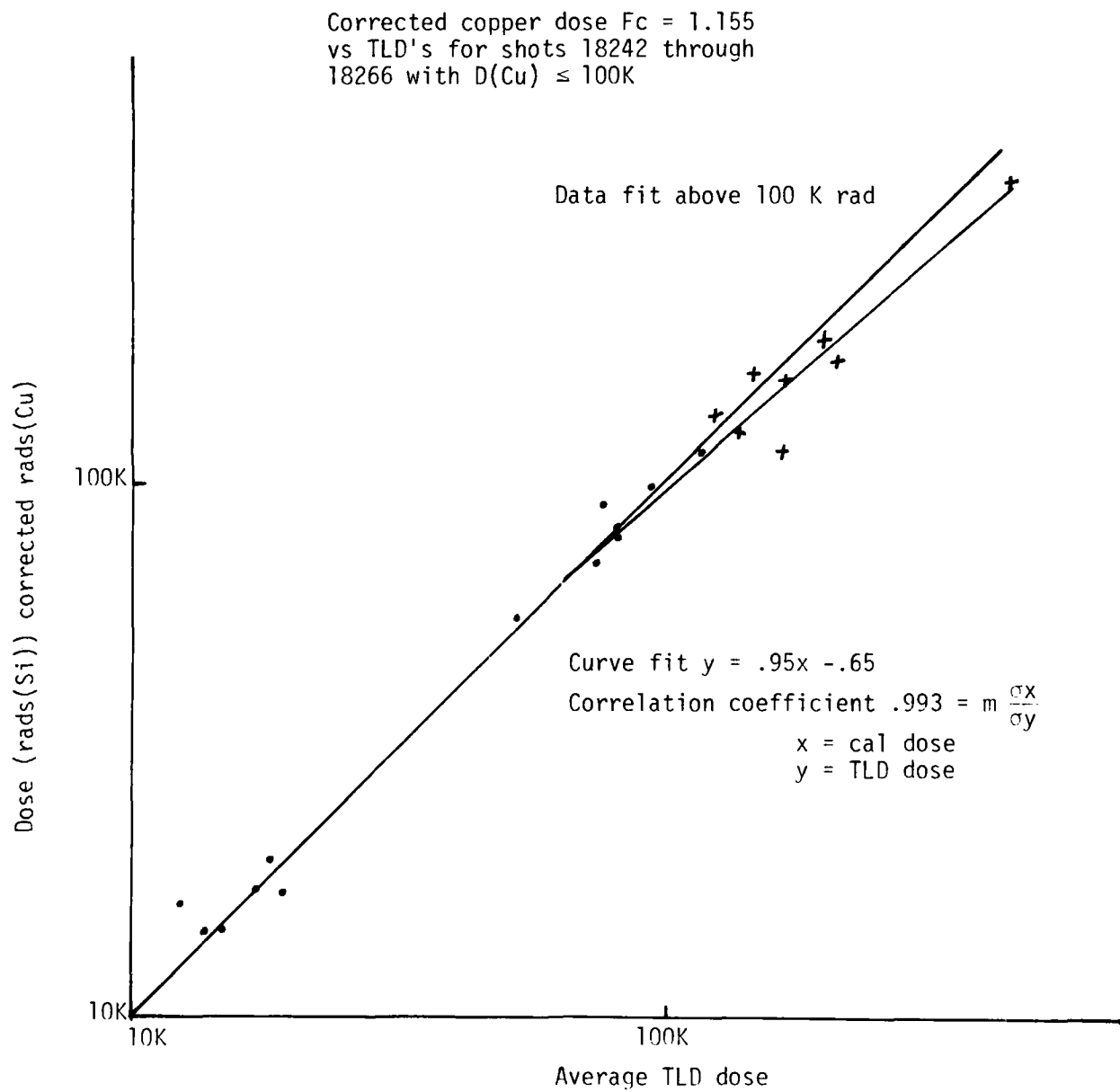


Figure 6. Comparison between TLD response and the copper calorimeter response.

Table 4. Comparison of copper calorimeter response to the TLD response at Hermes

Shot #	Copper Calorimeter Dose rad(Si)	TLD Dose rad(Si)
18213	$5.6 \times 10^4$	$1.4 \times 10^5$
18215	$1.3 \times 10^5$	$2.3 \times 10^5$
18216	$2.5 \times 10^4$	$5 \times 10^4$
18219	$1.2 \times 10^5$	$2.4 \times 10^5$
18220	$1.8 \times 10^5$	$3.6 \times 10^5$
18221	$1.1 \times 10^5$	$1.9 \times 10^5$
18223	$2.1 \times 10^5$	$3.5 \times 10^5$
18224	$2.2 \times 10^5$	$3.8 \times 10^5$
18225	$9.1 \times 10^4$	$2.9 \times 10^5$
18226	$8.5 \times 10^4$	$2.4 \times 10^5$
18227	$4.8 \times 10^5$	$1.2 \times 10^5$
18229	$8.3 \times 10^4$	$1.9 \times 10^5$
18230	$6.6 \times 10^4$	$1.4 \times 10^5$
18231	$1.1 \times 10^5$	$1.7 \times 10^5$
18232	$5.0 \times 10^4$	$6.2 \times 10^4$
18233	$2.3 \times 10^4$	$2.7 \times 10^4$
18234	$3.3 \times 10^4$	$3.1 \times 10^4$
18235	$3.1 \times 10^4$	$2.6 \times 10^4$
18236	$1.4 \times 10^4$	$1.2 \times 10^4$
18237	$2.1 \times 10^5$	$2.5 \times 10^5$
18238	$6.1 \times 10^4$	$6 \times 10^4$
18239	$1.2 \times 10^5$	$2.1 \times 10^5$

Table 4. (continued)

Dose	Copper Calorimeter Dose rad(Si)	TLD Dose rad (Si)
18240	$1.6 \times 10^5$	$2.0 \times 10^5$
18241	$1.1 \times 10^5$	$2.9 \times 10^5$
18242	$1.9 \times 10^4$	$1.7 \times 10^4$
18243	$1.4 \times 10^4$	$1.5 \times 10^4$
18244	$1.7 \times 10^4$	$1.7 \times 10^4$
18245	$1.6 \times 10^4$	$1.2 \times 10^4$
18248	$1.4 \times 10^4$	$1.3 \times 10^4$
18249	$7.1 \times 10^4$	$7.4 \times 10^4$
18250	$9.1 \times 10^4$	$7.4 \times 10^4$
18252	$1.2 \times 10^5$	$1.2 \times 10^5$
18253	$1.4 \times 10^5$	$1.7 \times 10^5$
18254	$1.1 \times 10^5$	$1.4 \times 10^5$
18255	$1.0 \times 10^5$	$1.6 \times 10^5$
18256	$1.4 \times 10^5$	--
18257	$1.5 \times 10^5$	$2.1 \times 10^5$
18258	$1.7 \times 10^4$	$1.8 \times 10^4$
18259	$7.1 \times 10^4$	$8.0 \times 10^4$
18260	--	--
18261	$1.0 \times 10^5$	$1.2 \times 10^5$
18262	$3.2 \times 10^5$	$4.3 \times 10^5$
18263	--	--
18264	$4.9 \times 10^4$	$5.2 \times 10^4$
18265	$8.5 \times 10^4$	$9.1 \times 10^4$
18266	$1.6 \times 10^5$	$2.0 \times 10^5$

To summarize, acceptable dose measurements can be performed at high intensities if the dosimeters are placed in close proximity to the device under test by using either calorimeters or TLD's. To adequately determine the dose for highly diverging beams, devices should be instrumented with dosimeters front and rear.



### SECTION 3

#### ELECTRON BEAM TRANSPORT

Several methods and combinations were utilized to vary the test part dose exposure. These included varying the electron drift chamber length (at HIFX only), varying the beam aperture size, and varying the drift chamber pressure for the e-beam exposure tests. For the photon mode tests, the converter to test part distance was varied.

The variation of aperture size for HIFX is shown in Figure 7 and for Hermes in Figure 8. These show a decrease in dose with decreasing aperture size with the exception of the Hermes four inch aperture. The shots using the four inch aperture were anomalous low output double hump shots. The variation in dose with increasing drift chamber length at HIFX showed a weak inverse length dependence. The dose decreased from  $6.4 \times 10^4$  rads(Si)/pulse for a 15 cm drift chamber length to  $1.8 \times 10^4$  rad at the 160 cm position at high vacuum and no aperture. The gamma dose vs. distance for the Hermes facility is shown in Figure 9 and decreases with distance as expected.

The technique of varying the drift chamber pressure to accomplish variations in test part dose exposures was utilized at both the HIFX and the Hermes facilities as the primary method of dose variation. The responses measured at the HIFX facility are shown in Figure 10 and the response measured previously at the Hermes facility is shown in Figure 11. As can be seen from these figures, the responses at the two facilities are different. The HIFX response was the lowest in high vacuum, peaked at  $\sim 0.5$  Torr and decreased for increasing pressures to 85 Torr. It was also observed that if the pressure in the HIFX drift chamber was maintained by

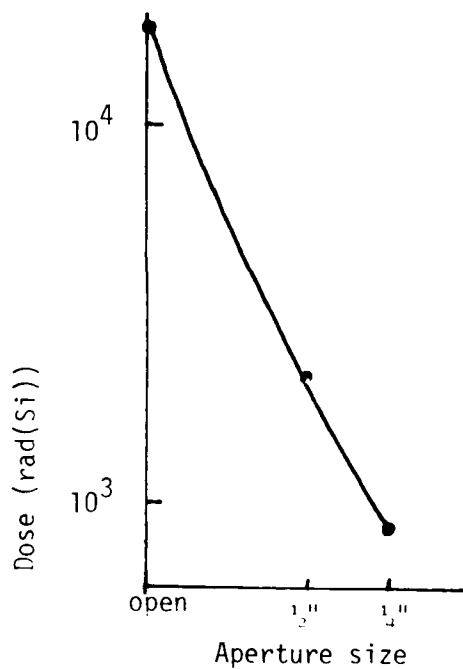


Figure 7. Dose variation vs aperture for HIFX-HiVac-160 cm position.

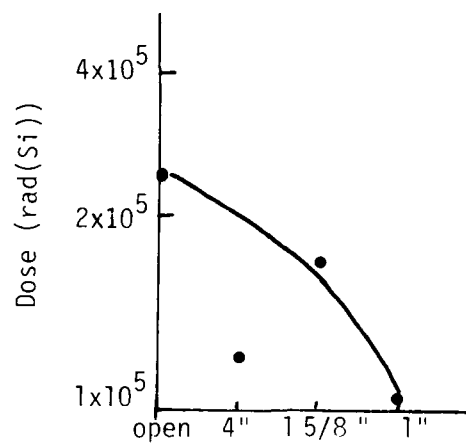


Figure 8. Dose variation vs aperture size for Hermes.



Figure 9. Hermes gamma dose vs distance.

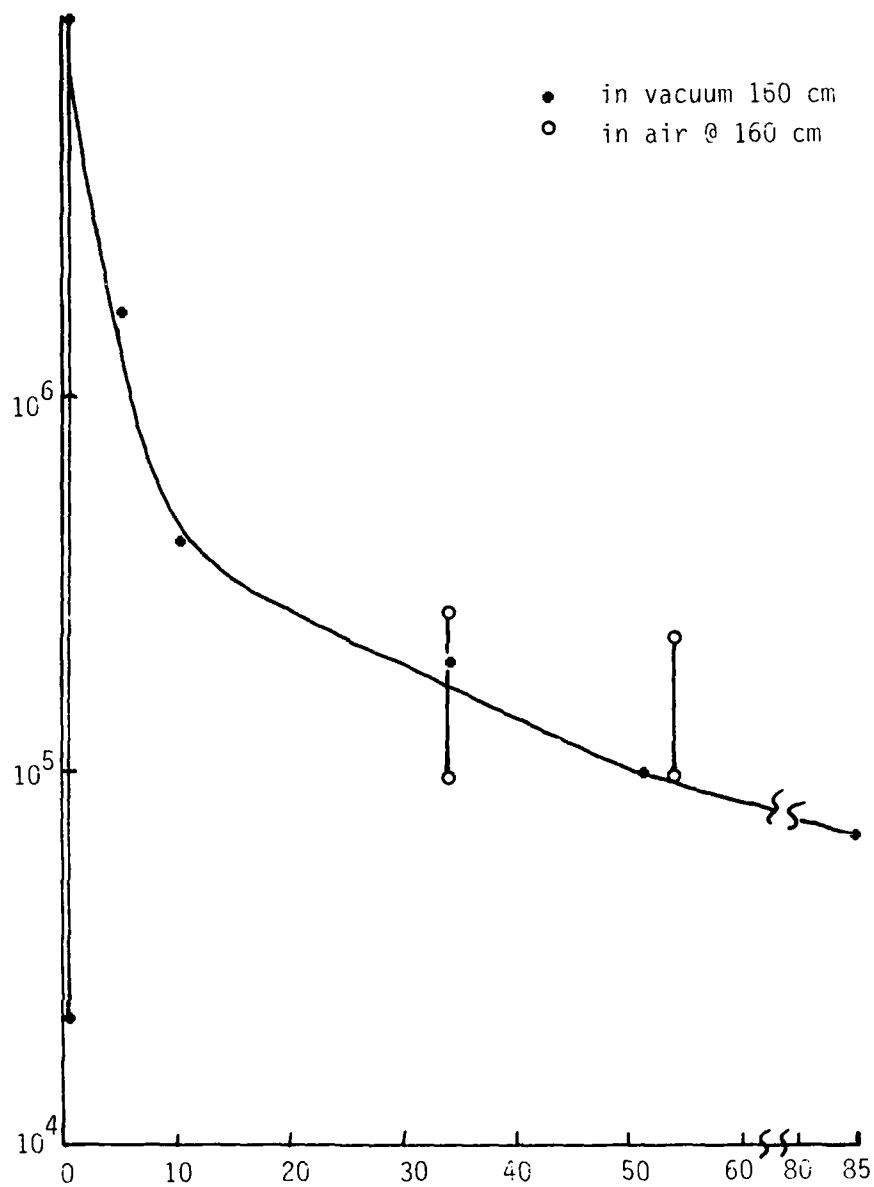


Figure 10. HIFX dose response vs. pressure.

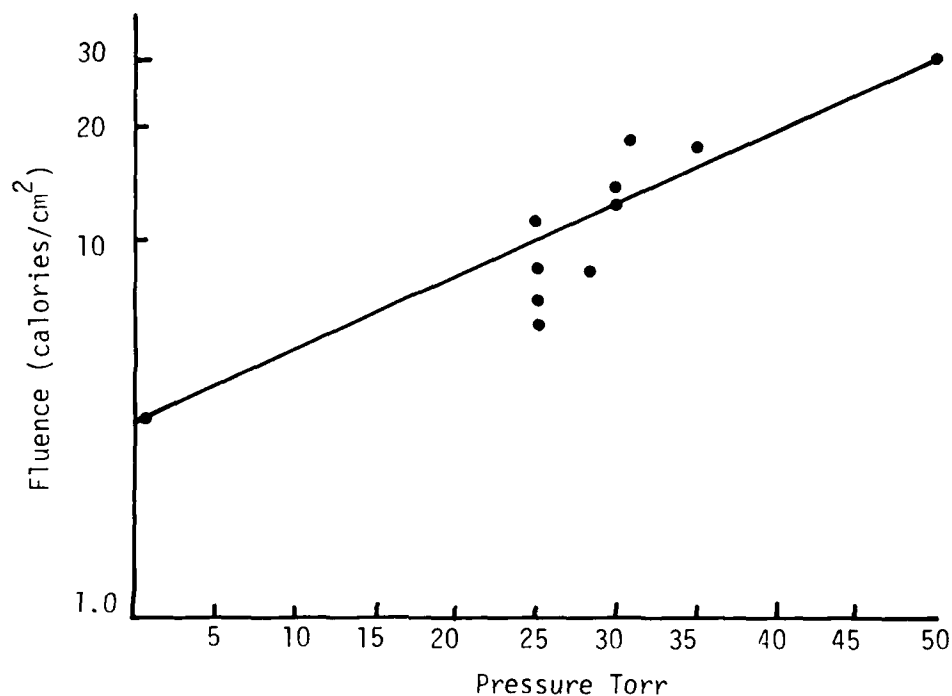


Figure 11. Hermes beam transport response vs pressure (from Sandia data shot #'s 17671 through 17680 + 17668).

sealing off the chamber, as opposed to pumping against a steady leak, that the dose on subsequent shots increased substantially. (These are the vertical bars in Figure 10). The Hermes response increased from 2 Torr (the lowest pressure operated at for Hermes) at higher pressures. In addition, at the HIFX facility, the diode was tested at atmospheric pressure air behind a thin drift chamber window as well as inside the drift chamber. Similar diode responses were obtained by both methods (see the Diode Test Section) however testing outside of a thin window proved to be more convenient and eliminated the problems of partial vacuum, air ionization interferences (caused by the 50V diode test bias level) when the diode was mounted inside the drift chamber.

To account for the observed differences in dose vs pressure at the Hermes and HIFX facilities, the effects of the electron beam propagation parameters on the beam propagation were examined and are presented below.

The radial electrostatic forces on an electron at the outer edge of a paraxial electron beam of length  $l$ , which is much greater than the beam diameter is given by,

$$F_r = q E_r = \frac{q I}{2\pi \beta a} \sqrt{\frac{\mu_0}{\epsilon_0}} \quad (8)$$

where  $q$  = electronic charge ( $1.6 \times 10^{-19}$  coulombs),  
 $E_r$  = radial electric field in volts per meter,  
 $\beta$  =  $v/c$ ,  
 $I$  = electron beam current,  
 $a$  = the electron beam diameter,  
 $\mu_0$  = permeability of free space, and  
 $\epsilon_0$  = permittivity of free space.

The radial electrostatic force on an electron at the outer edge of a column of ions is the negative of equation 8 since the electrostatic force is attractive. Therefore, the net Coulombic force on an outer edge electron is given by,

$$F_r = \frac{q I}{2\pi \beta a} \sqrt{\frac{\mu_0}{\epsilon_0}} (1 - f), \quad (9)$$

where we have defined the quantity  $f$  to be the ratio of ion to electron densities. When  $f = 1$  the beam is space charge neutralized.

Similarly, the radial magnetic force on an outer electron due to the magnetic field of the electron beam is given by,

$$F_r = - \frac{q \beta I}{2\pi a} \sqrt{\frac{\mu_0}{\epsilon_0}} \quad (10)$$

The net force (electrostatic and magnetic), per electron, on an outer edge electron can be expressed as,

$$\frac{F_{\text{net}}}{\text{electron}} = \frac{I}{2\pi a \beta} \sqrt{\frac{\mu_0}{\epsilon_0}} (\beta^2 - 1 + f). \quad (11)$$

Since the electron drift chambers utilized was only partially evacuated, the electron beams would also scatter outwardly. An expression for the worst case RMS scattering angle ( $\theta$ ), traversing a scattering material of thickness  $t$  (in  $\text{gm/cm}^2$ ) which is thin compared to the electron range, is given by equation 12 below where  $E_s$  is 21.2 Mev (the characteristic energy for scattering in air),  $t'$  is in units of  $36.5 \text{ gm/cm}^2$  and  $p$  is the electron momentum.

$$\langle \theta^2 \rangle = \frac{E_s^2 t'}{(pv)^2} \quad (\text{Ref. 1}) \quad (12)$$

Therefore using  $\rho = 1.7 \times 10^{-6} \text{ g/(cm}^3 \text{ Torr)}$  for the density of air we obtain

$$\langle \theta^2 \rangle = \frac{4.6 \cdot 10^4 \sqrt{1 - \beta^2} \sqrt{P}}{2 m_0 c^2} \quad (13)$$

where  $P$  is in Torr,  $t$  (the thickness of the scattering media) in meters and  $pv$  is equal to  $\beta^2 E$ . The angle theta ( $\langle \theta^2 \rangle$ ) represents the RMS scattering angle for a gaussian distribution of the incident beam (see Figure 12).

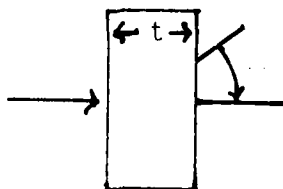


Figure 12. The geometry for multiple scattering through a foil of thickness  $t$ .

An electron exiting a scatterer at an angle,  $\theta$ , will have a radial component of velocity as well as an axial component. Therefore, the equivalent force which acted on the electron to accelerate it to its final radial velocity can be calculated. It is evident from Figure 12 that the radial component of velocity is the axial component times the  $\tan \theta$ . Therefore

$$v_r = v_z \tan \theta \quad (14)$$

the equivalent force,  $F = ma = mdV/dt$  where  $dV = V_r$  and  $dt =$  the time of flight through the scattering medium. If we assume relativistic electrons and small angles of  $\theta$  then  $\Delta t = \ell/c$  where  $\ell$  is the length of the chamber and  $c$  is the velocity of light. Therefore,

$$F = \beta m \frac{v_z \tan \theta}{\ell/c} \approx \frac{mc v_z \tan \theta}{\ell} \quad (15)$$

Rearranging terms we obtain, for the equivalent scattering force,

$$F_s = \frac{m_0 c^2 \beta^2 \tan \theta}{\sqrt{1 - \beta^2} \ell} \approx \frac{m_0 c^2 \beta^2 \theta}{\sqrt{1 - \beta^2} \ell} \quad (16)$$

where  $\tan \theta \approx \theta$  for small  $\theta$  was used. Using Equation 13 for  $\theta$  we obtain

$$F_s \sim 4.6 \times 10^4 \sqrt{P/\ell} \text{ ev/meter.} \quad (17)$$

Therefore the net total force on an outer edge electron due to Coulomb, magnetic and the equivalent scattering forces can be expressed as

$$\begin{aligned} F_{\text{net}} &= \frac{I}{2\pi a\beta} \sqrt{\frac{\mu_0}{\epsilon_0}} (\beta^2 - 1 + f) - \frac{m_0 c^2 \beta^2}{\sqrt{1 - \beta^2} \ell} \\ &= \left( \frac{60 I}{a \beta} (\beta^2 - 1 + f) - 4.6 \times 10^4 \sqrt{P/\ell} \right) \text{ ev/meter.} \quad (18) \end{aligned}$$

It is of interest to assess the machine parameter effects on the net force as expressed in Equation 18. The parameters in Equation 18, which have a strong machine dependence are  $f$  (the ratio of ion to electron density),  $I$  (the beam current),  $m_0 c^2 / \sqrt{1 - \beta^2}$  (the mean electron energy) and  $l$  (the drift chamber length).

To calculate the pressure at which space charge neutralization occurs ( $f = 1$  in Equation 18) early enough in the pulse ( $Q \sim 0.1 Q_{\max}$ ) to affect transport, the number of ions produced as a function of pressure must be known.

The density of electrons in the drift chamber is given by

$$n_e \approx \frac{I f}{q c v} \quad (19)$$

and the total number of electrons to pass through the drift chamber is given by

$$n_t = \frac{I}{q} t_{pw} \quad (20)$$

where  $t_{pw}$  is the pulse width.

The number of ions generated is given by the stopping power in air times the density of air divided by the energy loss per ion pair, times the total number of electrons ( $n_t$ ) times the chamber length. Therefore the ion density is given by

$$n_i = \frac{n_t}{v} = S_p \cdot 4.8 \times 10^{-2} \frac{P \cdot n_t}{v} \quad (21)$$

where  $S_p = 1.9 \times 10^2$  eV m<sup>2</sup>/g for Hermes and  $1.6 \times 10^2$  eV-m<sup>2</sup>/g for HIFX,  $P$  is the drift chamber pressure in Torr,  $l$  is the drift chamber length in



meters and  $n_t$  is given by equation 20 above. This results in the expression for  $f$  of

$$f = \frac{\rho_i}{\rho_e} = 4.8 \times 10^{-2} S_p t_{pw} c \quad (22)$$

Therefore  $f = 137$  P for Hermes where  $t_{pw} \approx 50$  ns and  $f = 58$  P for HIFX where  $t_{pw} \approx 25$  ns. If we add requirement that the beam becomes space charge neutral at  $Q = 0.1 Q_{max}$  we obtain space charge neutralization at  $\approx 0.07$  Torr for Hermes and  $\approx 0.17$  Torr for HIFX.

At higher pressures (after space charge neutralization is achieved) the effects of beam scattering can become significant. For comparison purposes, using a pressure of 100 Torr for both facilities, we obtain an equivalent scattering force of  $4.6 \times 10^5$  eV/meter for Hermes ( $\ell = 1$  meter) and  $3.6 \times 10^5$  eV/meter for HIFX ( $\ell = 1.6$  meter). Although this force is small in comparison to the magnetic force, it causes the beam to diverge. The magnetic force confines diverging electrons into spiral paths (which increases the path length and hence the effects of scattering) but does not provide any focusing action on the beam. These differences could explain the differences recorded at the HIFX and Hermes facilities.

In summary, these tests have demonstrated that dose variations can be conveniently and reliably achieved by variation of the drift chamber pressure. The techniques of variation of drift chamber length and aperture variation are less convenient and can be time consuming.

## DIODE TEST

The purpose of the diode test was to provide a test device of minimal complexity to validate the test methods and the dosimetry methods used for the various environments at the two facilities. The 1N916 is a high frequency diffused diode of simple rectangular geometry and is therefore an ideal device for this purpose.

It is desirable to completely shield the test circuit from the radiation. However, this requires long connecting leads to the device under test which introduces parasitic inductance and capacitance forming a resonant circuit. If the resonance is excited by the rise time of the photo current response (which follows the rise time of the radiation pulse), then the circuit will oscillate. Such a response obtained at HIFX is shown in Figure 13. This required shortening the connecting leads to such a degree that minimal circuit shielding was possible at HIFX. Therefore, it was found necessary to reduce the radiation induced interference signal by using a back-to-back transformer configuration as shown in Figure 14. At the Hermes facility, the rise time of the radiation pulse was longer allowing longer connecting leads and some circuit shielding. The Hermes rise time was approximately 2.5 times longer than the HIFX rise time. However, the back-to-back transformer configuration was also utilized at the Hermes facility.

A pair of diode responses obtained at HIFX are shown in Figure 15. As can be seen the two signals are not symmetrical, as would be the case in the absence of an interference. A differential amplifier was used to cancel the interference and a typical response is shown in Figure 16 which shows the photo current on the vertical axis ( $I_V = I_A$ ) and the time on the horizontal axis. The photo charge is then obtained by measuring the area under the curve, ( $I \cdot t = Q$  in Coulombs) and dividing by two.

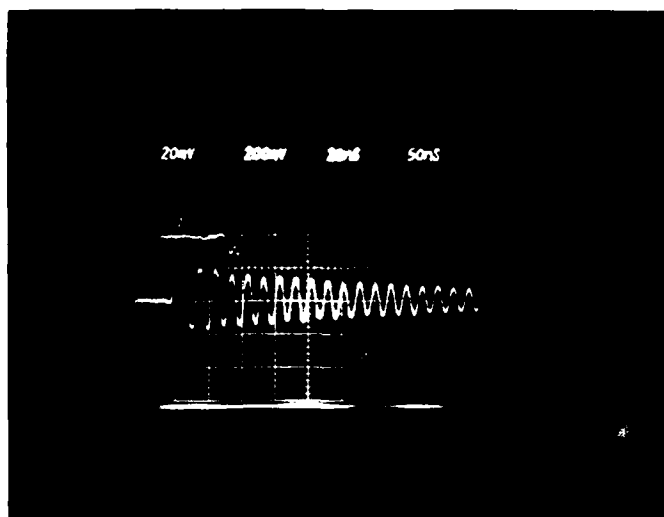


Figure 13. Photo response for a long lead measurement circuit.

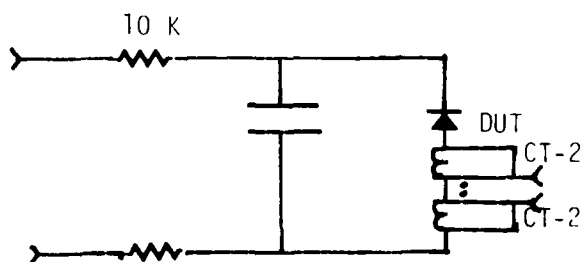


Figure 14. Double CT-2 test circuit.

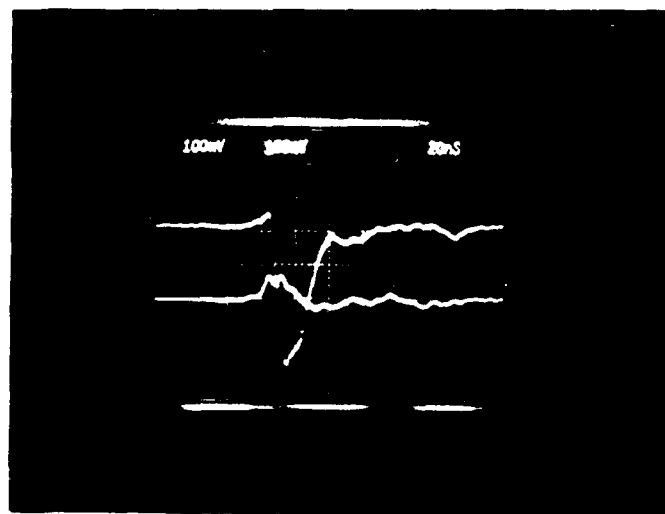


Figure 15. Double transformer outputs for HIFX shot #3031. Upper trace is transformer 1 and the lower trace is transformer 2.

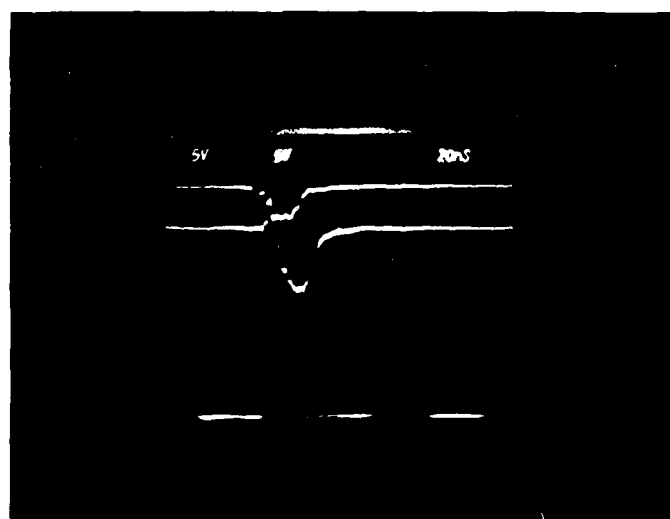


Figure 16. Differential photo response for HIFX shot #3052 (lower trace).

It was also found that to avoid large error signals coupled into the test device that ground planes were required between the device under test and any dielectric materials. The dielectrics charge up and noise could be capacitively coupled to the device under test. For these tests, the calorimeters were mounted in plastic holders and had to be isolated in this manner. When the devices were tested in the gamma mode, the cables required shielding in order to minimize their contribution to the observed response. A short coax cable will have a radiation response similar to a fast diode. In addition, a dummy diode (open) was used as an indicator of air ionization and cable-current contributions to the signal.

A determination of the expected photo response for the 1N916 device is useful. The U.K. personnel measured the photo response at  $\approx 1.4 \times 10^{-12}$  Coulombs/rad(Si). The photo response of a 1N914 diode which is similar to the 1N916 (except for twice the junction capacitance) has an average photo response of  $1 \times 10^{-12}$  Coulomb/rad(Si). It is also useful to calculate the theoretical response from the physical parameters of the diode. This was done using a measured junction area of  $2.6 \times 10^{-4} \text{ cm}^2$ , an assumed background doping density of  $4 \times 10^{15}$  (from the 100 V breakdown and a leakage current of 10 na at 50 V). The calculated value was  $2.4 \times 10^{-12}$  Coulomb/rad(Si) which is in the ball park of the other estimations.

The photo response versus dose (in rad(Si)) obtained at the HIFX and Hermes facilities is shown in Figure 17. The best linear straight line fit for the centrally weighted data, resulted in an average photo response of  $1.5 \times 10^{-12}$  Coulomb/rad(Si) with a correlation factor of 0.98. This is in good agreement with the predicted response.

Data excluded from the response were those obtained with an unshielded thermocouple feedthrough for the dose measurements and those data obtained at bias levels other than 50 V.

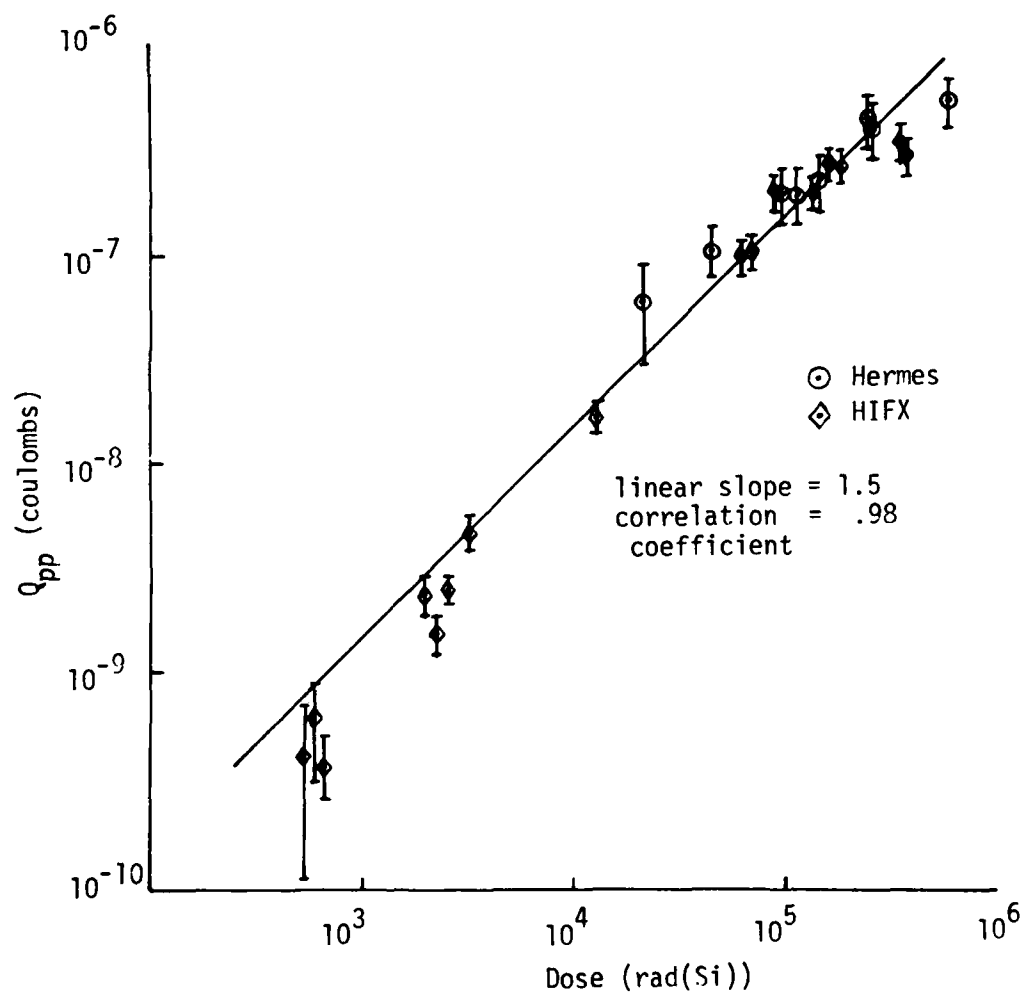


Figure 17. Summary plot of the Hermes and HIFX photo response.

In addition the e-beam results obtained at HIFX where the diode was mounted inside the drift chamber agreed quite well with those e-beam data obtained with the diode mounted outside the thin window. These results are tabulated in Table 5 for each type of exposure.

Table 5. Diode response for electron beam exposure in partial vacuum and atmospheric pressure air.

HIFX Shot #	$Q_{pp}/\text{rad}$	Exposure Environment
3044	$1.2 \times 10^{-12}$	Atmospheric Air
3045	$2 \times 10^{-12}$	
3046	$2.1 \times 10^{-12}$	
3048	$1.5 \times 10^{-12}$	
3049	$1.8 \times 10^{-12}$	
	$\bar{X} = 1.8 \times 10^{-12}$ $\sigma = 0.47 \times 10^{-12}$	
3051	$1.3 \times 10^{-12}$	Partial Vacuum
3052	$1.5 \times 10^{-12}$	
3053	$2.6 \times 10^{-12}$	
3054	$1.4 \times 10^{-12}$	
	$\bar{X} = 1.7 \times 10^{-12}$ $\sigma = 0.6 \times 10^{-1}$	

## SECTION 4

### CONCLUSIONS

This program has demonstrated test techniques and methods for high dose rate testing using FXR machines operated in the e-beam mode. It was found that the dose measured by either TLD's or calorimeters were in agreement if the devices were positioned in close proximity to each other. It was also found that the e-beam irradiated diode response agreed with the photon irradiated diode response. In addition, concerning the diode tests, it was shown that the results obtained when the diode was mounted inside the drift chamber (partial vacuum) or high vacuum agreed with the results obtained outside the drift chamber at atmospheric pressure. Since the atmospheric pressure measurements are more easily performed (they do not require vacuum feedthroughs) and are less subject to air ionization interference signal, they are preferred.

Finally, it was demonstrated that a convenient method of dose variation was accomplished by varying the drift chamber pressure, which changes the beam propagation parameters. This method is more convenient than changing aperture or the drift chamber length.



## DISTRIBUTION LIST

### DEPARTMENT OF DEFENSE

Assistant to the Secretary of Defense  
Atomic Energy

ATTN: Executive Assistant

Command & Control Technical Center

ATTN: C-362, G. Adkins

Defense Advanced Rsch Proj Agency

ATTN: J. Fraser  
ATTN: R. Reynolds

Defense Electronic Supply Center

ATTN: DEFC-ESA

Defense Logistics Agency

ATTN: DLA-SE  
ATTN: DLA-DEL, J. Slattery

Defense Nuclear Agency

ATTN: RAEV (TREE)  
4 cy ATTN: TITL

Defense Technical Information Center

12 cy ATTN: DD

Field Command

Defense Nuclear Agency  
ATTN: FCP

Field Command

Defense Nuclear Agency  
Livermore Branch  
ATTN: FCPRI

National Security Agency

ATTN: P. Deloy  
ATTN: T. Brown  
ATTN: G. Daily

NATO School (SHAPE)

ATTN: U.S. Documents Officer

Under Secretary of Defense for Rsch & Engrg

ATTN: Strategic & Space Sys (OS)

### DEPARTMENT OF THE ARMY

BMD Advanced Technology Center

Department of the Army  
ATTN: ATC-O, F. Hoke  
ATTN: ATC-T

BMD Systems Command

Department of the Army  
ATTN: BMDSC-HW, R. DeKalb

Deputy Chief of Staff for Rsch Dev & Acq

Department of the Army  
ATTN: Advisor for RDA Analysis, M. Gale

U.S. Army Armament Rsch Dev & Cmd

ATTN: DRDAR-LCA-PD

U.S. Army Communications R&D Command

ATTN: D. Huewe

### DEPARTMENT OF THE ARMY (Continued)

Harry Diamond Laboratories

Department of the Army  
ATTN: DELHD-N-RBH, J. Halprin  
ATTN: DELHD-N-RBH, H. Eisen  
ATTN: DELHD-N-RBC, J. McGarrity  
ATTN: DELHD-N-P  
ATTN: DELHD-N-RBH

U.S. Army Material & Mechanics Rsch Ctr

ATTN: DRXMR-H, J. Hofmann

U.S. Army Missile Command

3 cy ATTN: RSIC

U.S. Army Nuclear & Chemical Agency

ATTN: Library

White Sands Missile Range

Department of the Army  
ATTN: STEWS-TE-AN, T. Leura  
ATTN: STEWS-TE-AN, M. Squires

### DEPARTMENT OF THE NAVY

Naval Air Systems Command

ATTN: AIR 350F

Naval Electronic Systems Command

ATTN: Code 5045.11, C. Suman

Naval Ocean Systems Center

ATTN: Code 4471

Naval Postgraduate School

ATTN: Code 1424, Library

Naval Research Laboratory

ATTN: Code 6601, A. Wolicki  
ATTN: Code 6627, C. Guenzer  
ATTN: Code 6816, D. Patterson  
ATTN: Code 6816, H. Hughes  
ATTN: Code 6600, J. McEllinney  
ATTN: Code 5213, J. Killiany

Naval Sea Systems Command

ATTN: SEA-06J, R. Lane

Naval Surface Weapons Center

ATTN: Code F31  
ATTN: Code F30

Naval Weapons Center

ATTN: Code 233

Naval Weapons Evaluation Facility

ATTN: Code AT-6

Naval Weapons Support Center

ATTN: Code 7024, T. Ellis  
ATTN: Code 70242, J. Munarin  
ATTN: Code 7024, J. Ramsey

Office of Naval Research

ATTN: Code 220, D. Lewis  
ATTN: Code 427, L. Cooper

DEPARTMENT OF THE NAVY (Continued)

Office of the Chief of Naval Operations  
ATTN: OP 985F

Strategic Systems Project Office  
Department of the Navy  
ATTN: NSP-27331, P. Spector  
ATTN: NSP-230, D. Gold  
ATTN: NSP-2701, J. Pitsenberger  
ATTN: NSP-2015

DEPARTMENT OF THE AIR FORCE

Air Force Aeronautical Lab  
ATTN: LTE  
ATTN: LPO, R. Hickmott

Air Force Geophysics Laboratory  
ATTN: SULL S-29  
ATTN: SULL

Air Force Institute of Technology  
ATTN: ENP, J. Bridgeman

Air Force Systems Command  
ATTN: DLCAM  
ATTN: DLW  
ATTN: DLCA  
ATTN: XRLA

Air Force Technical Applications Ctr  
ATTN: TAE

Air Force Weapons Laboratory  
Air Force Systems Command  
ATTN: NTYC, Mullis  
ATTN: NTYC, Capt Swenson  
5 cy ATTN: NTYC

Air Force Wright Aeronautical Lab  
ATTN: POD, P. Stover

Air Force Wright Aeronautical Lab  
ATTN: TEA, R. Conlin  
ATTN: ORE

Air Logistics Command  
Department of the Air Force  
ATTN: MMEDD  
ATTN: DU-ALC/MM  
ATTN: MMET+

Assistant Chief of Staff  
Studies & Analyses  
Department of the Air Force  
ATTN: AF/SAMI

Ballistic Missile Office  
Air Force Systems Command  
ATTN: ENSN, H. Ward

Ballistic Missile Office  
Air Force Systems Command  
ATTN: ENMG  
ATTN: ENBE  
ATTN: ENSN, J. Tucker  
ATTN: SYOT

DEPARTMENT OF THE AIR FORCE (Continued)

Foreign Technology Division  
Air Force Systems Command  
ATTN: PDJV  
ATTN: TQTD, B. Ballard

Headquarters Space Division  
Air Force Systems Command  
ATTN: AQT, W. Blakney  
ATTN: AQM

Headquarters Space Division  
Air Force Systems Command  
ATTN: SZJ, R. Davis

Rome Air Development Center  
Air Force Systems Command  
ATTN: RBRP, C. Lane

Rome Air Development Center  
Air Force Systems Command  
ATTN: ETS, R. Dolan  
ATTN: ESER, R. Buchanan  
ATTN: ESR, P. Vail  
ATTN: ESR, W. Shedd  
ATTN: ESE, A. Lahar

Strategic Air Command  
Department of the Air Force  
ATTN: OPEN, M. Lanza

Tactical Air Command  
Department of the Air Force  
ATTN: OPS

DEPARTMENT OF ENERGY

Department of Energy  
ATTN: WASH

OTHER GOVERNMENT AGENCIES

Central Intelligence Agency  
ATTN: OSAR/NEO  
ATTN: OSAR/STO/MED, A. Puget

Department of Commerce  
National Bureau of Standards  
ATTN: Sec Ofc for J. Humphreys  
ATTN: Sec Ofc for S. Galloway  
ATTN: Sec Ofc for J. French

NASA  
Goddard Space Flight Center  
ATTN: V. Danchenko  
ATTN: J. Adolphsen

NASA  
George C. Marshall Space Flight Center  
ATTN: L. Haniter  
ATTN: EG02  
ATTN: M. Nowakowski

NASA  
ATTN: J. Murphy

OTHER GOVERNMENT AGENCIES (Continued)

NASA  
Lewis Research Center  
ATTN: M. Baddour

NASA  
Ames Research Center  
ATTN: G. DeYoung

DEPARTMENT OF ENERGY CONTRACTORS

Lawrence Livermore National Lab  
ATTN: Technical Info Dept, Library

Los Alamos National Laboratory  
ATTN: J. Freed

Sandia National Lab  
ATTN: R. Gregory  
ATTN: J. Barnum  
ATTN: J. Hood  
ATTN: F. Coppage  
ATTN: W. Dawes

DEPARTMENT OF DEFENSE CONTRACTORS

Advanced Research & Applications Corp  
ATTN: L. Palcuti  
ATTN: R. Armistead

Aerojet Electro-Systems Co  
ATTN: D. Toomb

Aerospace Corp  
ATTN: S. Bower  
ATTN: D. Fresh  
ATTN: R. Crolus

Aerospace Industries Assoc of America, Inc  
ATTN: S. Siegel

Battelle Memorial Institute  
ATTN: R. Thatcher

BDM Corp  
ATTN: D. Wunch  
ATTN: D. Alexander  
ATTN: R. Pease

Bendix Corp  
ATTN: E. Meeder

Boeing Co  
ATTN: D. Egelkrout

Boeing Co  
ATTN: W. Rumpza  
ATTN: C. Rosenberg  
ATTN: I. Arimura  
ATTN: A. Johnston

Burr-Brown Research Corp  
ATTN: H. Smith

California Institute of Technology  
ATTN: W. Price  
ATTN: A. Stanley  
ATTN: A. Shumka

DEPARTMENT OF DEFENSE CONTRACTORS (Continued)

Charles Stark Draper Lab, Inc  
ATTN: C. Lai  
ATTN: R. Bedingfield  
ATTN: P. Greiff  
ATTN: R. Ledger  
ATTN: Tech Library  
ATTN: A. Schutz  
ATTN: A. Freeman

Cincinnati Electronics Corp  
ATTN: C. Stump  
ATTN: L. Hammond

University of Denver  
ATTN: F. Venditti

E-Systems, Inc  
ATTN: K. Reis

Electronic Industries Association  
ATTN: J. Hessman

Ford Aerospace & Communications Corp  
ATTN: J. Davison  
ATTN: Technical Information Services

Franklin Institute  
ATTN: R. Thompson

Garrett Corp  
ATTN: R. Weir

General Dynamics Corp  
ATTN: W. Hansen

General Dynamics Corp  
ATTN: O. Wood  
ATTN: R. Fields

General Electric Co  
ATTN: J. Peden  
ATTN: R. Casey  
ATTN: J. Andrews

General Electric Co  
ATTN: J. Palchefskey, Jr  
ATTN: Technical Library  
ATTN: R. Benedict  
ATTN: R. Casey  
ATTN: W. Patterson

General Electric Co  
ATTN: J. Reidl

General Electric Co  
ATTN: R. Hellen

General Electric Co  
ATTN: J. Gibson  
ATTN: D. Cole

General Electric Co  
ATTN: D. Pepin

General Research Corp  
ATTN: Technical Information Office  
ATTN: R. Hill

DEPARTMENT OF DEFENSE CONTRACTORS (Continued)

Georgia Institute of Technology  
ATTN: R. Curry

Goodyear Aerospace Corp  
ATTN: Security Control Station

Grumman Aerospace Corp  
ATTN: J. Rogers

Harris Corporation  
ATTN: J. Cornell  
ATTN: C. Anderson  
ATTN: T. Sanders

Honeywell, Inc  
ATTN: R. Gumm

Honeywell, Inc  
ATTN: C. Cerulli

Honeywell, Inc  
ATTN: Technical Library

Hughes Aircraft Co  
ATTN: R. McGowan  
ATTN: J. Singletary

Hughes Aircraft Co  
ATTN: A. Narevsky  
ATTN: D. Shumake  
ATTN: W. Scott  
ATTN: E. Smith

IBM Corp  
ATTN: H. Mathers  
ATTN: T. Martin

IBM Corp  
ATTN: MS 110-036, F. Tietze

IIT Research Institute  
ATTN: I. Mindel

Institute for Defense Analyses  
ATTN: Tech Info Services

International Business Machine Corp  
ATTN: J. Ziegler

International Tel & Telegraph Corp  
ATTN: A. Richardson  
ATTN: Dept 608

IRT Corp  
ATTN: N. Rudie  
ATTN: J. Harrity

JAYCOR  
ATTN: L. Scott  
ATTN: T. Flanagan  
ATTN: R. Stahl

Johns Hopkins University  
ATTN: P. Partridge

Kaman Sciences Corp  
ATTN: J. Lubell  
ATTN: N. Beauchamp  
ATTN: M. Bell

DEPARTMENT OF DEFENSE CONTRACTORS (Continued)

Kaman Tempo  
ATTN: M. Espig  
ATTN: DASIAC

Kaman Tempo  
ATTN: DASIAC

Litton Systems, Inc  
ATTN: J. Retzler

Lockheed Missiles & Space Co, Inc  
ATTN: J. Crowley  
ATTN: J. Smith

Lockheed Missiles & Space Co, Inc  
ATTN: E. Hessee  
ATTN: E. Smith  
ATTN: M. Smith  
ATTN: P. Bene  
ATTN: D. Phillips  
ATTN: C. Thompson

M.I.T. Lincoln Lab  
ATTN: P. McKenzie

Martin Marietta Corp  
ATTN: H. Cates  
ATTN: S. Bennett  
ATTN: R. Gaynor  
ATTN: W. Brockett  
ATTN: W. Janocko

Martin Marietta Corp  
ATTN: E. Carter

McDonnell Douglas Corp  
ATTN: Library  
ATTN: M. Stich  
ATTN: D. Dohm  
ATTN: R. Kloster

McDonnell Douglas Corp  
ATTN: D. Fitzgerald  
ATTN: J. Holmgren

McDonnell Douglas Corp  
ATTN: Technical Library

Mission Research Corp  
ATTN: C. Longmire  
5 cy ATTN: Document Control

Mission Research Corp  
ATTN: R. Pease

Mission Research Corp, San Diego  
ATTN: J. Raymond  
ATTN: V. Van Lint  
4 cy ATTN: T. Wrobel

Mission Research Corporation  
ATTN: W. Ware

Mitre Corp  
ATTN: M. Fitzgerald

Motorola, Inc  
ATTN: A. Christensen

DEPARTMENT OF DEFENSE CONTRACTORS (Continued)

Motorola, Inc  
ATTN: O. Edwards

National Academy of Sciences  
ATTN: National Materials Advisory Board  
ATTN: R. Shane

National Semiconductor Corp  
ATTN: A. London  
ATTN: R. Wang

Norden Systems, Inc  
ATTN: D. Longo  
ATTN: Technical Library

Northrop Corp  
ATTN: J. Srou

Northrop Corp  
ATTN: P. Gardner  
ATTN: L. Apodaca  
ATTN: T. Jackson

Pacific-Sierra Research Corp  
ATTN: H. Brode

Physics International Co  
ATTN: J. Shea  
ATTN: Division 6000

R & D Associates  
ATTN: S. Rogers  
ATTN: P. Haas

Rand Corp  
ATTN: C. Crain

Raytheon Co  
ATTN: J. Ciccio

Raytheon Co  
ATTN: H. Flescher  
ATTN: A. Van Doren

RCA Corp  
ATTN: G. Brucker  
ATTN: V. Mancino

RCA Corp  
ATTN: D. O'Connor  
ATTN: Office N103

RCA Corp  
ATTN: R. Killion

RCA Corp  
ATTN: W. Allen

Rensselaer Polytechnic Institute  
ATTN: R. Gutmann

Research Triangle Institute  
ATTN: Sec Ofc for M. Simons, Jr

Rockwell International Corp  
ATTN: J. Brandford  
ATTN: V. De Martino  
ATTN: V. Michel  
ATTN: V. Strahan

DEPARTMENT OF DEFENSE CONTRACTORS (Continued)

Rockwell International Corp  
ATTN: TIC BA08  
ATTN: T. Yates

Rockwell International Corp  
ATTN: D. Vincent

Sanders Associates, Inc  
ATTN: L. Brodeur

Science Applications, Inc  
ATTN: D. Long  
ATTN: J. Naber  
ATTN: V. Verbinski  
ATTN: V. Ophan

Science Applications, Inc  
ATTN: W. Chadsey

Science Applications, Inc  
ATTN: D. Stribling

Singer Co  
ATTN: J. Brinkman

Singer Co  
ATTN: R. Spiegel

Sperry Rand Corp  
ATTN: Engineering Laboratory

Sperry Rand Corp  
ATTN: F. Scaravaglione  
ATTN: C. Craig  
ATTN: R. Viola  
ATTN: P. Marffino

Sperry Rand Corp  
ATTN: D. Schow

Sperry Univac  
ATTN: J. Inda

Spire Corp  
ATTN: R. Little

SRI International  
ATTN: P. Dolan  
ATTN: B. Gasten  
ATTN: A. Whitson

Sylvania Systems Group  
ATTN: L. Pauples  
ATTN: C. Thornhill  
ATTN: L. Blaisdell

Sylvania Systems Group  
ATTN: H & V Group  
ATTN: P. Fredrickson  
ATTN: J. Waldron  
ATTN: H. Ullman

Systron-Donner Corp  
ATTN: J. Indelicato

Teledyne Ryan Aeronautical  
ATTN: J. Rawlings

DEPARTMENT OF DEFENSE CONTRACTORS (Continued)

Texas Instruments, Inc  
ATTN: R. Stehlin  
ATTN: A. Peletier

TRW Defense & Space Sys Group  
ATTN: A. Pavelko  
ATTN: O. Adams  
ATTN: P. Guilfoyle  
ATTN: H. Holloway  
ATTN: A. Witteles  
ATTN: R. Kingsland

TRW Defense & Space Sys Group  
ATTN: F. Fay  
ATTN: M. Gorman  
ATTN: R. Kitter  
ATTN: W. Willis, M/S RI/2078

DEPARTMENT OF DEFENSE CONTRACTORS (Continued)

Vought Corp  
ATTN: R. Tomme  
ATTN: Technical Data Center  
ATTN: Library

Westinghouse Electric Co  
ATTN: L. McPherson

Westinghouse Electric Corp  
ATTN: H. Kalapaca  
ATTN: D. Crichi